Supporting Information

d^2 ion-doped Vacancy-Ordered Double Perovskites as Broadband NIR Scintillators for Radiation Detection

Bing-Jun Zhu, Jiacheng Liu, Yang (Michael) Yang, En Ma, Jia-Jun Yan , Heng-Yun Ye* and Le-Ping Miao*

1. Experimental Section:

1.1. Materials

CsCl (Heowns, 99%), $ZrCl_4$ (3AChem, 98%), $MoCl_5$ (adamas-beta, 99.6%), WCl_4 (adamas-beta, 99.9%), Hydrochloric acid (Jiangxi Xinguang, 37 wt%), Methanol (Tianjin Damao, 99.5%). All materials were used directly without further processing.

1.2. Growth of Cs_2ZrCl_6 Single Crystal

The single crystal was obtained by a simple hydrothermal reaction (Figure S1a). 2 mmol CsCl and 1 mmol $ZrCl_4$ powder were added into a 25 ml polytetrafluoroethylene-lined reactor, and 7 ml hydrochloric acid was added and mixed evenly. The stainless steel reactor was maintained at 190°C for 48 h and then cooled to room temperature at a cooling rate of 0.5°C h^{-1} to obtain single crystals. The product was washed with methanol and dried at 60°C for 7 h for subsequent characterization.

1.3. Growth of Mo^{4+} and W^{4+}-doped Cs_2ZrCl_6 Single Crystal

There is no difference between the synthesis of the d^2 ions-doped compound and the original material, except that the amount of $ZrCl_4$ substance becomes 1-x mmol, where x is the doping amount of $MoCl_5$/WCl_4. It is worth noting that $MoCl_5$ will be reduced to Mo^{4+} in hydrochloric acid, which is the source of Mo^{4+}-doped in the sample. It has already been established in similar studies that $MoCl_5$ undergoes reduction to the +4 oxidation state in hydrochloric acid [1]. Furthermore, the fact that the positions of the transition peaks observed in the samples discussed in the main text correspond to the Tanabe-Sugano diagram for a d^2 electron configuration serves as additional corroborating evidence that the ionic oxidation state is +4.

1.4. Preparation of Transparent Flexible Thin Films

Cs_2ZrCl_6: Mo^{4+}@PDMS flexible film was prepared by the spin coating method. 6 g of PDMS and 0.6 g of homogenized sample powder were mixed by ultrasonication and stirring to form a uniform colloidal mixture. The mixture was degassed in a vacuum environment, and then the colloidal mixture was spin-coated onto a

quartz substrate at 700 rpm. The spin-coated samples were cured by heating at 120 °C for 12 h, and the transparent flexible film could then be peeled off the quartz substrate for imaging.

2. Characterization:

2.1. Structural characterization

The phase purity of the samples was determined by the Empyrean brand X-ray diffraction instrument (PANalytical B.V., Netherlands) equipped with a Cu anode (40 kV, 40 mA, $\lambda = 1.5406$ Å). Diffraction data were collected in continuous scanning mode in the range of $2\theta = 5°$ to 80° with a step size of $2\theta = 0.02°$ and a scan speed maintained at 3° min^{-1}. The refinement of the unit cell parameters was performed using the Rietveld method by the GSAS software [2]. The X-ray photoelectron spectra (XPS) were recorded on a PHI 5000 VersaProbe III photoelectron spectrometer (PHI, Japan) with an Argon sputter ion gun (0-5 keV continuously adjustable) as the X-ray source. The microstructure of the samples was recorded by scanning electron microscopy (SEM, MLA650F, American FEI), and the distribution of each element in the samples was described by SEM energy dispersive spectrometer (EDS) mapping.

2.2. Optical properties

The absorption spectra of the sample are measured on a UV-Vis-NIR spectrophotometer (UV-3600i Plus, Shimadzu, Japan). The steady-state photoluminescence (PL) and photoluminescence excitation (PLE) spectra of the samples were recorded by a fluorescence spectrophotometer (FLS980, Edinburgh, England) equipped with a Xe-lamp as the light source. The sample was sandwiched between two quartz sample holders and placed in the spectrometer to determine the maximum excitation and emission peak positions. At the determined positions, the sample PL decay dynamics were monitored.

2.3. Theoretical simulation details

The electronic band structures and partial density of states (DOS) of all samples were calculated by the CASTEP module based on density functional theory (DFT) implemented in Materials Studio 2020 [3]. The structural model of Cs_2ZrCl_6 was directly imported from the cif file, and the structural model of the doped sample was obtained by replacing one Zr^{4+} in $Cs_8Zr_4Cl_{24}$ with Mo^{4+}/W^{4+}. The generalized gradient approximation (GGA) of the PedewBurke-Emzerhof (PBE) function with projected augmented wave (PAW) is used to describe the exchange correlation interaction [4]. At the same time, due to the strong correlation effect of TM, DFT+U is used to improve the calculation accuracy of the strongly correlated system. The kinetic energy cutoff of 600 eV, the convergence tolerance of 1.0×10^{-6} eV $atom^{-1}$, the force tolerance of 0.01 eV $Å^{-1}$, the maximum displacement of 0.002 Å, and the maximum stress of 0.1 GPa were selected in the calculations. The Brillouin zone was sampled with a

2×2×2 *k*-point Monkhorst-Pack grid [5].

2.4. Scintillation performance

RL spectra and scintillation-related performance are measured on a variable temperature X-ray spectrometer test system (X-XILS-P70V-5, Xiamen XingZheKeChuang Co., Ltd., China).

3. Calculation details or formula：

3.1 Optical band gap

The band gap energy of a semiconductor can be measured by the Tauc-plot method [6]:

$$(\alpha h\nu)^{1/n} = B(h\nu - E_g) \#(S1)$$

where α is the absorption coefficient, h is the Planck constant, ν is the photon frequency, B is the comparison constant, E_g is the band gap energy, and n is a constant describing the properties of electronic transitions. When the semiconductor is a direct bandgap, n=1/2; and when the semiconductor is an indirect bandgap, phonons are involved in the electron transition process, and the electrons will be scattered by the lattice, so phonons need to be introduced, n=2. From the simulation results, it can be found that both the undoped and d^2 ions-doped samples are direct bandgap semiconductors (n=1/2).

3.2. Calculation of the Racah inter-electron repulsion parameter B and crystal field splitting energy 10Dq of d^2 ion-doped Cs_2ZrCl_6

Take Mo^{4+} as an example; its spectrum data (Figure 2e):

E_1 ($^3T_{1g}$(P)-$^3T_{1g}$(F)) = 22172 cm^{-1},

E_2 ($^3T_{2g}$(F)-$^3T_{1g}$(F)) = 13605 cm^{-1},

E_3 (^1E_g(D)/$^1T_{2g}$(D)-$^3T_{1g}$(F)) = 10917 cm^{-1}.

So, E_1/E_2 = 1.63, E_1/E_3 = 2.03, and E_2/E_3 = 1.25.

For d^2 Tanabe-Sugano diagram is most consistent at the position of $10Dq/B$ = 23.

In this case, E_1/B = 34.1, E_2/B = 21.1, E_3/B = 15.5.

Taking the average of the values obtained from the three transitions, B_{avg} (Mo^{4+}) ≈ 666 cm^{-1}.

Dq = 23 × 666/10 = 1531.8 cm^{-1}.

Therefore, the crystal field splitting energy ($10Dq$) of Mo^{4+} under Cl^- octahedral coordination in Cs_2ZrCl_6 lattice is about 15318 cm^{-1}.

The same method is used for the correlation calculation of W^{4+}, the only difference is that the $^3A_{2g}$(F)-$^3T_{1g}$(F) transition energy is selected as E_1, and the result is B_{avg} (W^{4+}) = 643 cm^{-1}, $10Dq$ = 14789 cm^{-1}.

3.3. PL lifetime

Since the emission peak comes from the overlap of multiple excited states, the curve is fitted by a double exponential formula:

$$R(t) = A_1 e^{\left(-t/\tau_1\right)} + A_2 e^{\left(-t/\tau_2\right)} \#(S2)$$

where A_1 and A_2 are decay constants, and τ_1 and τ_2 refer to the decay lifetimes of the two exponential components. And the average lifetime of the sample is calculated by the following formula [7]:

$$\tau_{ave} = \frac{A_1\tau_1^2 + A_2\tau_2^2}{A_1\tau_1 + A_2\tau_2} \#(S3)$$

where A_1, A_2, τ_1, and τ_2 have exactly the same meanings as the parameters in Formula S2.

3.4. Activation energy of thermal quenching

The integrated PL intensity of temperature-dependent spectral variation of d^n ions can be revealed by the Arrhenius formula [8]:

$$I(T) = \frac{I_0}{1 + A\cdot\exp\left(-\frac{E_a}{k_B T}\right)} \#(S4)$$

where I_0 is the initial PL intensity, I(T) is the PL intensity at various temperatures, A is the fitting constant, k_B is the Boltzmann constant, and E_a is the activation energy of thermal quenching.

3.5. Huang-Rhys factor S

The strength of the electron-phonon coupling in the lattice can be obtained by the following formula [9]:

$$FWHM = 2.36\sqrt{S}E_{ph}\sqrt{coth\frac{E_{ph}}{2k_B T}} \#(S5)$$

where $E_{ph} = \hbar\omega_{phonon}$ represents the effective phonon temperature, k_B and T are the Boltzmann constant and temperature, respectively, and the Huang-Rhys factor S reflects the strength of the electron-phonon coupling interaction.

3.6. Calculation of X-ray Attenuation Efficiency

X-ray absorption is determined by the Beer-Lambert law [10]:

$$I = I_0 e^{-\alpha d} \#(S6)$$

where I is the intensity of the transmitted X-ray photon, I_0 is the initial intensity of the X-ray photon, α is the total attenuation coefficient, and d is the thickness of the active layer. Then the attenuation efficiency of the active layer with different thicknesses can be obtained:

$$Attenuation\ efficiency = \frac{I_0 - I}{I_0} = 1 - e^{-\alpha d} \#(S7)$$

3.7. Calculation of Light Yield

According to the above discussion, using a sample with a thickness far exceeding 0.5 mm, determining the X-rays are completely absorbed, the light yield of the sample is calculated by the RL spectrum of the commercial scintillator CsI: Tl (54000 photons·MeV^{-1}) and the sample according to the following equation [11-13]:

$$\frac{LY_{Cs_2NaYCl_6:Yb^{3+}}}{LY_{BGO}} = \frac{R_{Cs_2NaYCl_6:Yb^{3+}} \int I_{BGO}(\lambda)S(\lambda)d\lambda / \int I_{BGO}(\lambda)d\lambda}{R_{BGO} \int I_{Cs_2NaYCl_6:Yb^{3+}}(\lambda)d(\lambda)d\lambda / \int I_{Cs_2NaYCl_6:Yb^{3+}}(\lambda)d\lambda} \#(S8)$$

Here, R is the corrected response amplitude, I is the RL intensity at different wavelengths (λ), S is the wavelength dependent detection efficiency, and the X-rays are uniformly irradiated on the sample surface during the test.

3.8. Elongation equation δ

The stretch properties of flexible film are described by the elongation δ:

$$\delta = (L_H - L_0)/L_0 \#(S9)$$

where δ is the elongation, and L_H and L_0 are the lengths after stretching and the initial length, respectively.

3.9. Details of MTF measurement.

MTF reflects its ability to convert input signals at a given spatial frequency into output. This result reflects the fundamental spatial resolution performance of the imaging system. The spatial resolution is derived from the spatial frequency value when MTF = 0.2. The MTF was obtained using the slant-edge method. A 1 mm thick aluminum sheet with sharp edges was placed on the scintillator film, and an X-ray image of the edge profile was obtained by the imaging system. The edge spread function (ESF) is obtained from the image of the edge profile, and the line spread function (LSF) is further obtained from it. Finally, the value of MTF is defined by the Fourier transform of LSF [14]:

$$MTF(\nu) = F(LSF(x)) = F\left(\frac{dESF(x)}{dx}\right) \#(S10)$$

where ν is the spatial frequency, and x is the position of the image pixel.

4. Additional Figure:

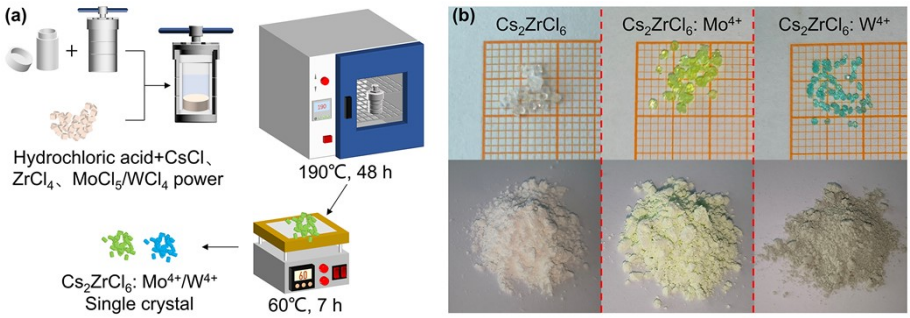

Figure S1. (a) Schematic diagram of the synthesis process of single crystals. (b) Photographs of undoped, Mo^{4+}-doped, and W^{4+}-doped Cs_2ZrCl_6 single crystals and corresponding powder samples.

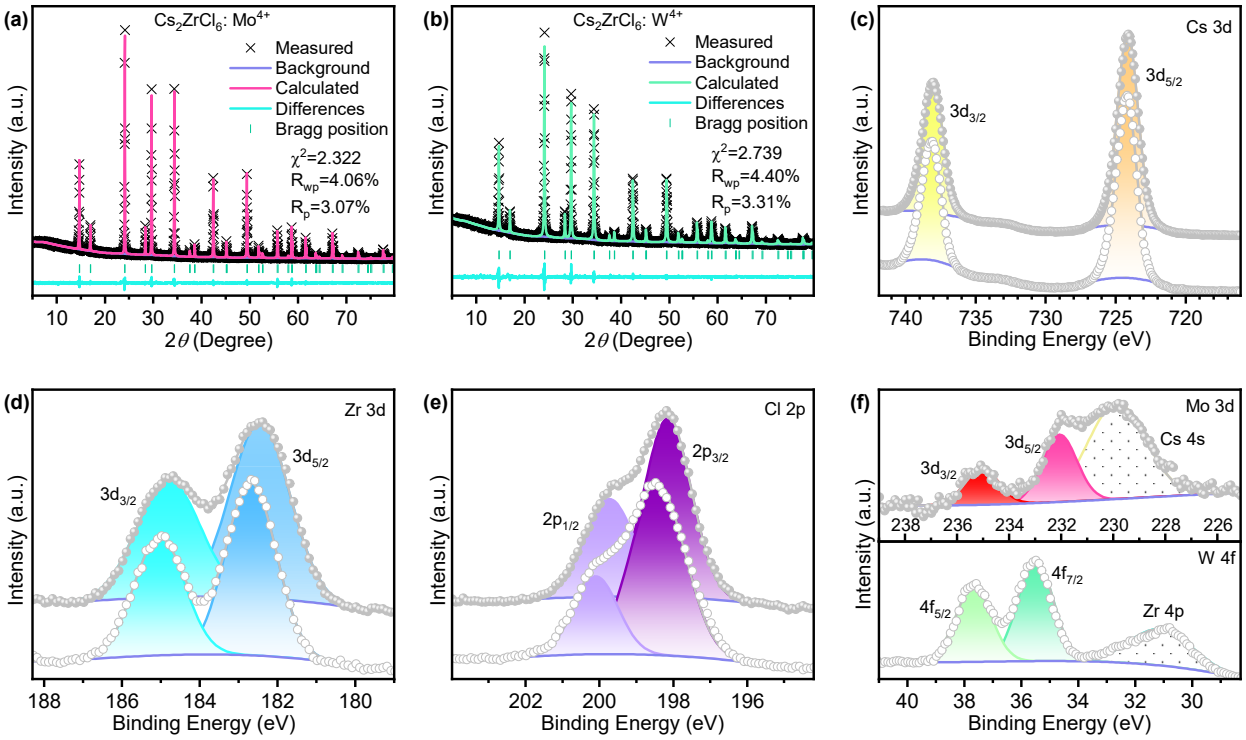

Figure S2. Rietveld refinement of XRD pattern of (a) Cs_2ZrCl_6: Mo^{4+} (15 mol%) and (b) Cs_2ZrCl_6: W^{4+} (15 mol%). High-resolution XPS spectra of (c) Cs, (d) Zr, (e) Cl, and (f) Mo/W atoms in Mo^{4+}-doped (gray dots) and W^{4+}-doped (white dots) Cs_2ZrCl_6.

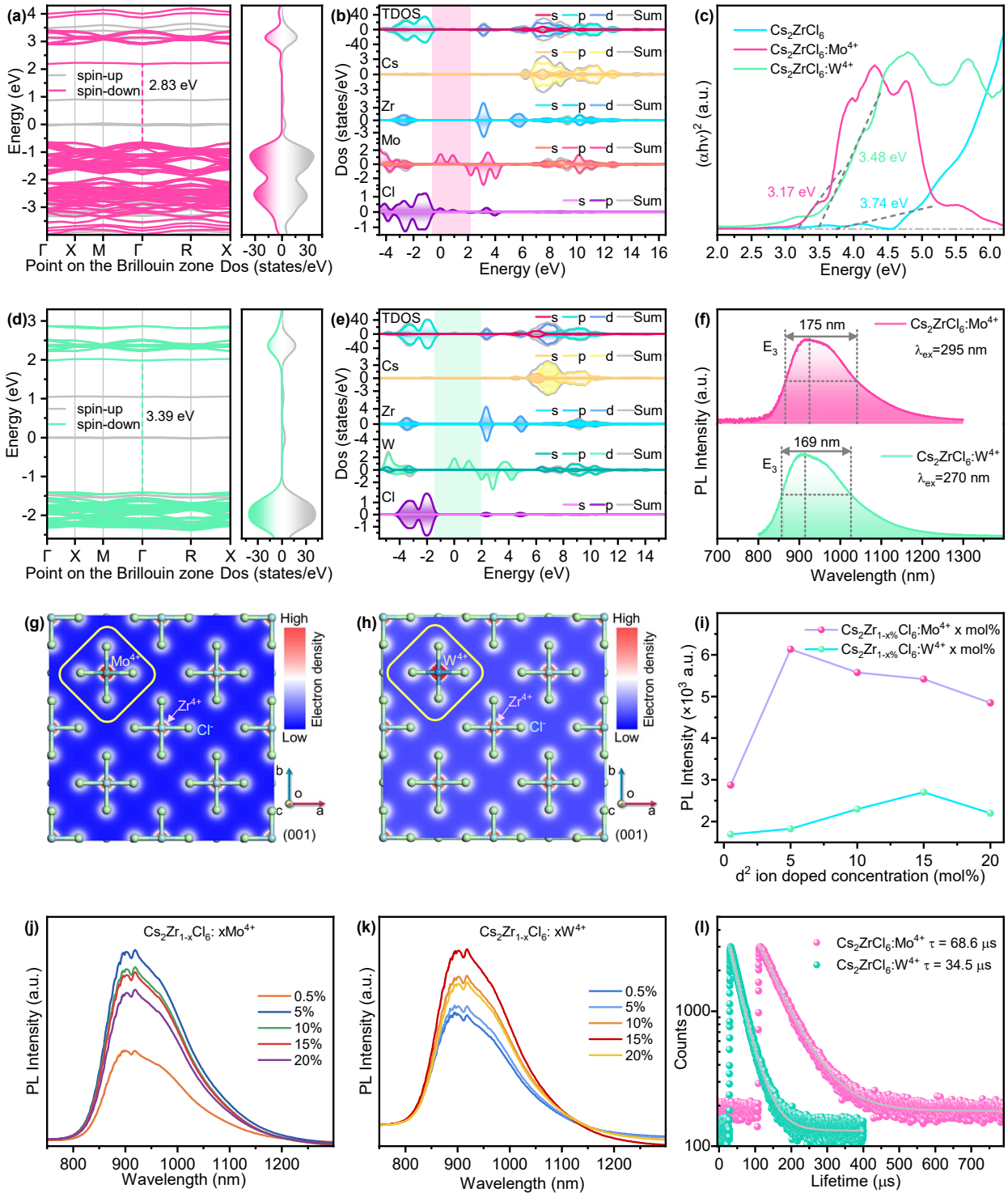

Figure S3. (a, d) Electronic band structure and (b, e) atom PDOS of Mo^{4+} and W^{4+}-doped Cs_2ZrCl_6, respectively. (c) Optical band gaps of undoped and Mo^{4+} (5 mol%)/W^{4+} (15 mol%)-doped Cs_2ZrCl_6 from the Tauc-plot method. (f) NIR PL spectra of Cs_2ZrCl_6: Mo^{4+} (5 mol%)/W^{4+} (15 mol%). Electron density isosurface at (001) facet of (g) Cs_2ZrCl_6: Mo^{4+} and (h) Cs_2ZrCl_6: W^{4+}. (i) Variation of PL intensity of d^2 ion-doped Cs_2ZrCl_6 with doping concentration. PL spectra of (j) $Cs_2Zr_{1-x}Cl_6$: xMo^{4+} and (k) $Cs_2Zr_{1-x}Cl_6$: xW^{4+} at different doping concentrations. (l) PL decay curve and the corresponding fitting curve of Cs_2ZrCl_6: Mo^{4+} (5 mol%)/W^{4+} (15

mol%).

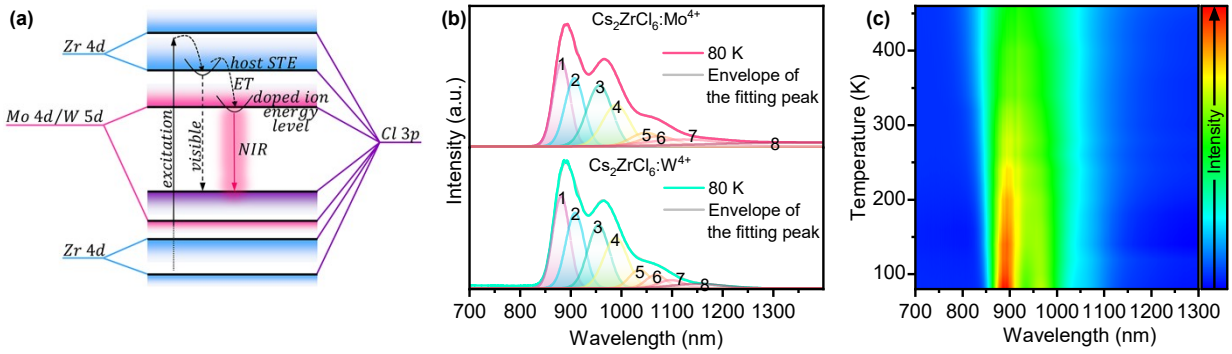

Figure S4. (a) Schematic energy diagram of Cs_2ZrCl_6: Mo^{4+}/W^{4+} and the excitation and emission processes caused by doping. (b) Deconvolution of the spectrum of Cs_2ZrCl_6: Mo^{4+} (5 mol%)/W^{4+} (15 mol%) measured at 80K to show that the broadband emission originates from multiple transitions. (c) Pseudo-color plot of the temperature-dependent PL spectra (excited at 270 nm) for Cs_2ZrCl_6: W^{4+} (15 mol%) measured in the range of 80-460 K.

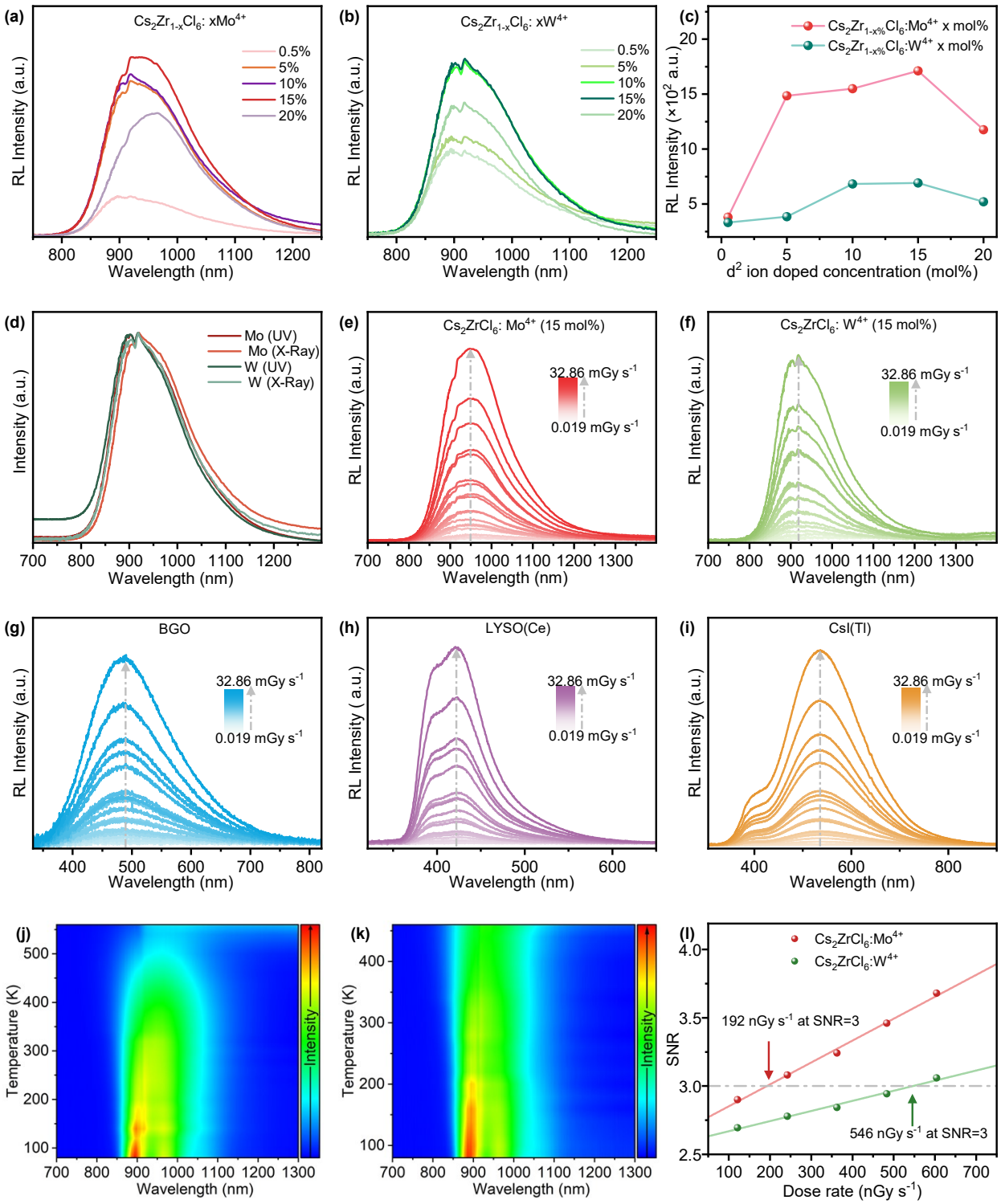

Figure S5. RL spectra of (a) $Cs_2Zr_{1-x}Cl_6$: xMo^{4+} and (b) $Cs_2Zr_{1-x}Cl_6$: xW^{4+} at different doping concentrations and (c) their relative intensity. (d) Normalized spectra of Cs_2ZrCl_6: Mo^{4+}(15 mol%) and Cs_2ZrCl_6: W^{4+}(15 mol%) under UV excitation (λ_{ex} = 295 nm and 270 nm, respectively) and under X-ray excitation (20 KeV, 3.7 mGy·s^{-1}). RL Spectra of (e) Cs_2ZrCl_6: Mo^{4+} (15 mol%), (f) Cs_2ZrCl_6: W^{4+} (15 mol%), (g) BGO, (h) LYSO: Ce, and (i) CsI: Tl measured at room temperature within the X-ray dose range of 19 μGy·s^{-1}-33 mGy·s^{-1}. Pseudo-color plot of the temperature-dependent RL spectra (20 KeV, 3.7 mGy·s^{-1}) for (j) Cs_2ZrCl_6: W^{4+} (15 mol%) and (k)

Cs_2ZrCl_6: W^{4+} (15 mol%). (l) Signal-to-noise ratio (SNR) as a function of X-ray dose rate of sample.

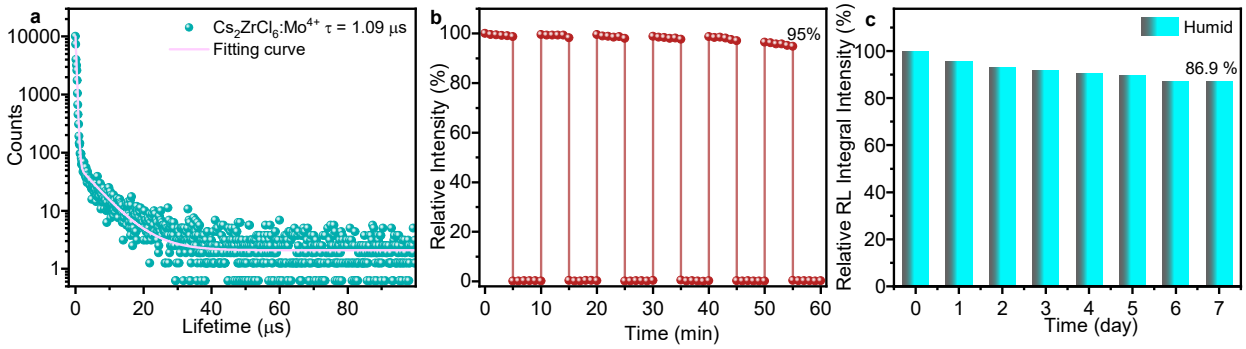

Figure S6. (a) RL decay curve and the corresponding fitting curve of Cs_2ZrCl_6: Mo^{4+} (5 mol%). (b) RL intensity of Cs_2ZrCl_6: W^{4+} within one hour of 20 kV-20 mA X-ray (3.7 $mGy \cdot s^{-1}$) irradiation. (c) Long-term stability of RL (20 keV) intensity of Cs_2ZrCl_6: Mo^{4+}@PDMS under humid (completely immersed in water).

5. Additional Table:

Table S1. Comparison of feeding molar concentration of each element in Mo^{4+}(15%)-doped Cs_2ZrCl_6 with actual concentrations determined by XPS.

Cs_2ZrCl_6: Mo^{4+}(15 mol%)	Cs	Zr	Cl	Mo
Feeding Molar Ratio	22.22%	9.44%	66.66%	1.66%
XPS	22.19%	11.83 %	65.17%	0.81%

Table S2. Comparison of feeding molar concentration of each element in W^{4+}(15%)-doped Cs_2ZrCl_6 with actual concentrations determined by XPS.

Cs_2ZrCl_6: W^{4+}(15 mol%)	Cs	Zr	Cl	W
Feeding Molar Ratio	22.22%	9.44%	66.66%	1.66%
XPS	19.99%	12.42%	66.60%	1.00%

Table S3. Comparison of the performances in different scintillators for X-ray imaging

Scintillator	Wavelength (nm)	Light Yield (photons·MeV^{-1})	Detection Limit ($nGy_{air} \cdot s^{-1}$)	Spatial Resolution ($lp \cdot mm^{-1}$)	Flexible	Reference
$Cs_2Ag_{0.6}Na_{0.4}In_{1-y}Bi_yCl_6$	652	3900	19	4.4	No	[13]
$Cs_2Ag_{0.6}Na_{0.4}In_{0.95}Bi_{0.05}Cl_6$:Tm	800	33500	55.2	11.2	Yes	[15]
Cs_2HfCl_6:Mo^{4+}	900	44500	87.4	12	Yes	[16]
$CsPbCl_xBr_{3-x}$:Yb^{3+}	980	112000	176.5	-	No	[17]
Cs_2ZrX_6:Cr^{3+}	900	56250	31.2	7.7	No	[18]
Cs_2ZrX_6 (MA^+ and Br^-)	500	-	-	25.1	No	[19]

$Cs_2ZrCl_6:Mo^{4+}$	925	51613	192	10	Yes	This Work

References

1. Z. Li, M. Xu, W. Liu, X. Wang, Y. Li, X. Zhou, Z. Fang and L. Ning, Broadband Near-Infrared Luminescence from Mo^{4+} in Zero-Dimensional Perovskite $Cs_2Zr(Cl,Br)_6$ with an Exceptionally High Quantum Efficiency and Thermal Stability, *Chemistry of Materials*, 2024, **36**, 901-910.
2. B. Toby, EXPGUI, a graphical user interface for GSAS, *J. Appl. Crystallogr.*, 2001, **34**, 210-213.
3. S. J. Clark, M. D. Segall, C. J. Pickard, P. J. Hasnip, M. I. J. Probert, K. Refson and M. C. Payne, First principles methods using CASTEP, *De Gruyter Brill*, 2005, **220**, 567-570.
4. J. P. Perdew, K. Burke and M. Ernzerhof, Generalized Gradient Approximation Made Simple, *Phys. Rev. Lett.*, 1996, **77**, 3865-3868.
5. H. J. Monkhorst and J. D. Pack, Special points for Brillouin-zone integrations, *Phys. Rev. B*, 1976, **13**, 5188-5192.
6. S. He, Q. Qiang, T. Lang, M. Cai, T. Han, H. You, L. Peng, S. Cao, B. Liu, X. Jing and B. Jia, Highly Stable Orange-Red Long-Persistent Luminescent $CsCdCl_3:Mn^{2+}$ Perovskite Crystal, *Angew. Chem., Int. Ed.*, 2022, **61**, e202208937.
7. A. Abfalterer, J. Shamsi, D. J. Kubicki, C. N. Savory, J. Xiao, G. Divitini, W. Li, S. Macpherson, K. Galkowski, J. L. MacManus-Driscoll, D. O. Scanlon and S. D. Stranks, Colloidal Synthesis and Optical Properties of Perovskite-Inspired Cesium Zirconium Halide Nanocrystals, *ACS Mater. Lett.*, 2020, **2**, 1644-1652.
8. J. Zhou, X. Rong, M. S. Molokeev, Y. Wang, X. Yun, D. Xu and X. Li, Alloying Cs^+ into $Rb_2ZrCl_6:Te^{4+}$ toward highly efficient and stable perovskite variants, *Mater. Chem. Front.*, 2021, **5**, 4997-5003.
9. S. Saikia, A. Gopal, R. Rathod, A. Joshi, K. R. Priolkar, S. Saha, P. K. Santra, K. Shanmuganathan and A. Nag, Ultrabroad Near Infrared Emitting Perovskites, *Angew. Chem., Int. Ed.*, 2025, **64**, e202415003.
10. Q.-H. Zou, W.-H. Yang, L.-K. Wu, L.-L. Jiang, S.-H. Wang, L. Liu, R.-F. Li, H.-Y. Ye and J.-R. Li, Ionothermal synthesis of a stable three-dimensional Cu_4I_4 cluster scintillator with near-unity quantum efficiency and weak thermal quenching, *Inorg. Chem. Front.*, 2025, **12**, 692-700.
11. F. Cao, D. Yu, W. Ma, X. Xu, B. Cai, Y. M. Yang, S. Liu, L. He, Y. Ke, S. Lan, K.-L. Choy and H. Zeng, Shining Emitter in a Stable Host: Design of Halide Perovskite Scintillators for X-ray Imaging from Commercial Concept, *Acs Nano*, 2020, **14**, 5183-5193.
12. B. Yang, L. Yin, G. Niu, J.-H. Yuan, K.-H. Xue, Z. Tan, X.-S. Miao, M. Niu, X. Du, H. Song, E. Lifshitz and J.

Tang, Lead-Free Halide Rb_2CuBr_3 as Sensitive X-Ray Scintillator, *Adv. Mater.*, 2019, **31**, 1904711.

13. W. Zhu, W. Ma, Y. Su, Z. Chen, X. Chen, Y. Ma, L. Bai, W. Xiao, T. Liu, H. Zhu, X. Liu, H. Liu, X. Liu and Y. M. Yang, Low-dose real-time X-ray imaging with nontoxic double perovskite scintillators, *Light:Sci. Appl.*, 2020, **9**, 112-112.
14. H. Xu, W. Liang, Z. Zhang, C. Cao, W. Yang, H. Zeng, Z. Lin, D. Zhao and G. Zou, 2D Perovskite Mn^{2+}-Doped $Cs_2CdBr_2Cl_2$ Scintillator for Low-Dose High-Resolution X-ray Imaging, *Adv. Mater.*, 2023, **35**, 2300136.
15. C. Wang, J. Xiao, S. Ma, Y. Li and Z. Yan, Efficient Near-Infrared Emitting Halide Scintillators with Mitigating External Light Crosstalk for Portable X-Ray Imaging, *Advanced Functional Materials*, 2024, **34**, 2401995.
16. W. Liao, K. Han, Y. Wang and Z. Xia, Cs_2HfCl_6:Mo^{4+} as Near-Infrared-Emitting Scintillators for Dual-Mode Collaborative Imaging, *Laser & Photonics Reviews*, 2025, **19**, 2500311.
17. L. Zi, J. Song, N. Wang, T. Wang, W. Li, H. Zhu, W. Xu and H. Song, X-Ray Quantum Cutting Scintillator Based on $CsPbCl_xBr_{3-x}$:Yb^{3+} Single Crystals, *Laser & Photonics Reviews*, 2023, **17**, 2200852.
18. X. Li, J. Yan, T. T. Bezuneh, T. Kou, J. Xu, D. Yang, R. Luo, T. Chang, Q. Zhao, L. Wang and W. W. Yu, Lead-Free Halide Perovskite Cs_2ZrX_6 Doped with Cr^{3+} for Multifunctional X-ray and NIR Imaging, *Journal of Physical Chemistry Letters*, 2025, **16**, 9280-9287.
19. H. Wang, S. Zhang and Z. Xia, Composition Modulation of Cs_2ZrCl_6-based Scintillator Film via Vapor Deposition for Large-Area X-Ray Imaging, *Small Methods*, 2025, **9**, 2500273.